In Situ X-Ray Diffraction Studies on Structural Changes of a P2 Layered Material during Electrochemical Desodiation/Sodiation

*Young Hwa Jung, Ane S. Christiansen, Rune E. Johnsen, Poul Norby, and Do Kyung Kim**

Sodium layered oxides with mixed transition metals have received significant attention as positive electrode candidates for sodium-ion batteries because of their high reversible capacity. The phase transformations of layered compounds during electrochemical reactions are a pivotal feature for understanding the relationship between layered structures and electrochemical properties. A combination of in situ diffraction and ex situ X-ray absorption spectroscopy reveals the phase transition mechanism for the ternary transition metal system (Fe–Mn–Co) with P2 stacking. In situ synchrotron X-ray diffraction using a capillary-based microbattery cell shows a structural change from P2 to O2 in P2–$Na_{0.7}Fe_{0.4}Mn_{0.4}Co_{0.2}O_2$ at the voltage plateau above 4.1 V on desodiation. The P2 structure is restored upon subsequent sodiation. The lattice parameter *c* in the O2 structure decreases significantly, resulting in a volumetric contraction of the lattice toward a fully charged state. Observations on the redox behavior of each transition metal in P2–$Na_{0.7}Fe_{0.4}Mn_{0.4}Co_{0.2}O_2$ using X-ray absorption spectroscopy indicate that all transition metals are involved in the reduction/oxidation process.

1. Introduction

Rechargeable lithium-ion batteries (LIBs) have greatly changed our daily lives by providing mobile convenience to laptops, tablet PCs, smartphones, digital cameras, etc. The need for rechargeable batteries with high energy densities, long lifetimes, and low costs has increased with the increasing demand of electric vehicles (*x*EVs) and large energy storage systems (ESSs). To keep pace with inquiries for next-generation batteries, investigations on sodium-ion batteries (SIBs) have increased because of abundant resources and the low cost of Na. Because sodium ions have similar chemical properties to lithium ions in equivalent structures, knowledge of LIBs can be adapted almost directly to the sodium system. Sodium equivalents of lithium-containing electrode materials, such as oxides, sulfides, phosphates, pyrophosphates, fluorophosphates, and alloying metals, have been evaluated as electrode materials for SIBs.[1–6]

Among the positive electrode materials for SIBs, layered oxides ($NaTMO_2$, TM = transition metals) are most attractive due to their large capacity, simple synthesis, and structural stability.[7–14] Various transition metal elements can be substituted into the layered structure, similar to layered lithium compounds, and this will influence the structural stability of sodium-ion removal, operating voltage, capacity, and cyclability. In contrast to lithium systems, different stacking structures for Na layered oxides can be examined because of the preferred prismatic coordination of the larger sodium ions. Positive electrode materials with a P2 layered structure by Delmas' notation[15] have better cyclability and structural stability during electrochemical reactions than those with an O3 layered structure.[16] The trigonal prismatic site is more favorable for the diffusion of sodium ions,[17–20] and the diffusion kinetics for Na^+ can thus be more efficient in the P2 layered structure compared to those in the O3 layered structure, which is common in lithium intercalation compounds. P2 layered materials with various transition metal compositions for SIBs have been studied, such as Mn–Co, Ni–Mn, and Fe–Mn.[9,17,21–25] Moreover, several approaches for the doping of two-component P2 layered materials with transition metals have also been introduced,[8] including Co doping on Ni–Mn compounds,[26,27] Ni doping on Co–Mn systems,[28,29] and Ni doping on Fe–Mn system.[30] However, few studies on the Fe–Mn–Co system with P2 stacking have been reported compared to Ni–Fe–Mn or Ni–Co–Mn P2 materials.[31,32] Co can facilitate the oxidation of Fe atoms, as reported in Li compounds,[33] and Co can likely stabilize the oxidized state in the layered structure, especially for Fe-containing layered materials.[34] In addition, Wang et al. reported that Co suppresses the irreversibility of P2–$Na_{2/3}Mn_yCo_{1-y}O_2$ materials.[23] A similar behavior in the P2–Na–Fe–Co–Mn oxides would be expected.

In this paper, P2–$Na_{0.7}[(Fe_{0.5}Mn_{0.5})_{1-x}Co_x]O_2$ (x = 0, 0.05, 0.10, and 0.20) was synthesized by a solid-state reaction, and the electrochemical performance of the P2–Fe–Mn–Co system

Y. H. Jung, Prof. D. K. Kim
Department of Materials Science and Engineering
Korea Advanced Institute of
Science and Technology (KAIST)
291 Daehak-ro, Yuseong-gu,
Daejeon 305-701, Republic of Korea
E-mail: dkkim@kaist.ac.kr
A. S. Christiansen, R. E. Johnsen, Prof. P. Norby
Department of Energy Conversion and Storage
Technical University of Denmark
Roskilde DK-4000, Denmark

DOI: 10.1002/adfm.201500469

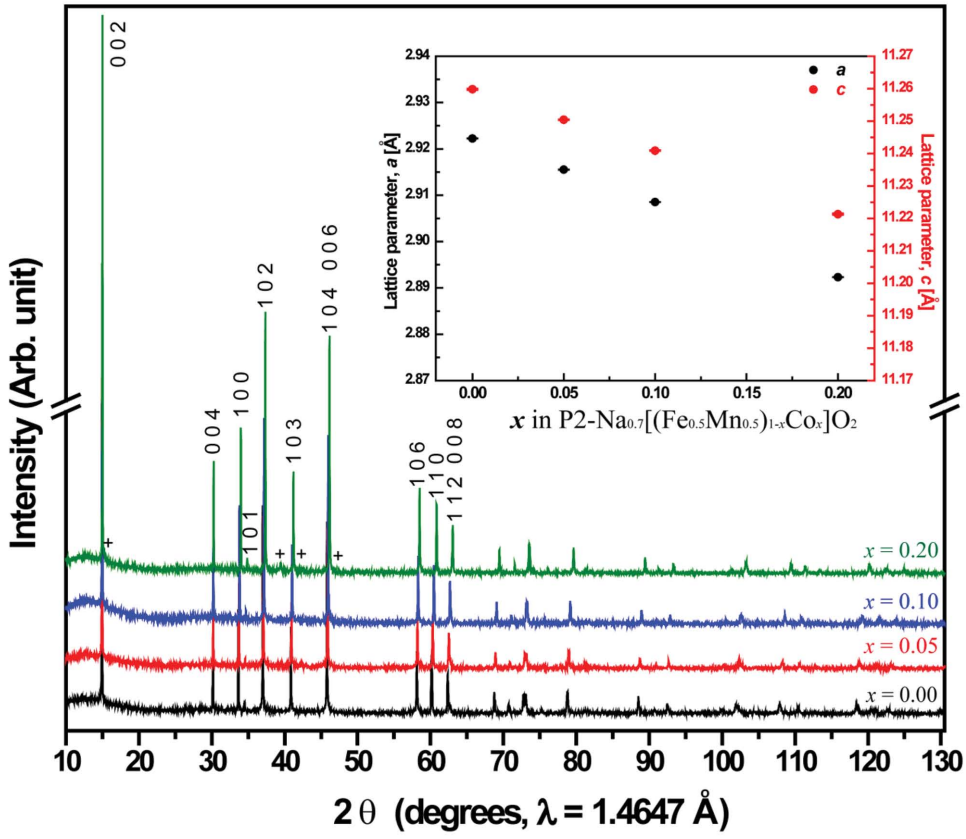

Figure 1. The synchrotron powder diffraction patterns of P2–$Na_{0.7}[(Fe_{0.5}Mn_{0.5})_{1-x}Co_x]O_2$ powders (x = 0, 0.05, 0.10, and 0.20). Inset shows the lattice parameter changes by contents of Co (x) in P2 layered materials. Cross marks correspond to the O3-impurity phase.

is reported. We performed in situ synchrotron X-ray diffraction (XRD) measurements on P2–$Na_{0.7}Fe_{0.4}Mn_{0.4}Co_{0.2}O_2$ during electrochemical sodiation and desodiation as a model system of an Fe–Co–Mn layered material. Ex situ X-ray absorption spectroscopy (XAS) investigated the redox couple of each transition metal during the electrochemical reactions. The effects of the phase stability and redox behaviors on the sodiation/desodiation processes are discussed based on these results.

2. Results and Discussion

2.1. Synthesis and Electrochemical Properties

The synchrotron XRD patterns of $Na_{0.7}[(Fe_{0.5}Mn_{0.5})_{1-x}Co_x]O_2$ (x = 0, 0.05, 0.10, and 0.20) were all indexed in the hexagonal lattice ($P6_3/mmc$, No. 194) identical to the P2 layered structure (**Figure 1**). The cell parameters and unit cell volume from the Rietveld refinement of the synchrotron XRD patterns of all samples are tabulated in **Table 1**, and each refined result from the diffraction pattern is depicted in Figure S1 (Supporting Information). A pure P2 phase is obtained by x = 0.33,[31] but small diffraction peaks corresponding to an O3 layered structure in *R-3m* were observed above x = 0.10. The amount of the O3-impurity phase in x = 0.20 was ≈2 wt%, and detailed structural parameters from Rietveld refinement for $Na_{0.7}Fe_{0.4}Mn_{0.4}Co_{0.2}O_2$ are summarized in **Table 2**. The inset of Figure 1 shows the cell parameter changes by the Co content (x). The value of a and c decreased when the Co content increased because of the smaller ionic radius of Co compared to that of Fe and Mn. The P2 layered material is an Na-deficient structure ($x \leq 0.7$); hence, the exact oxidation states of transition metal elements are not exactly +3. This will be discussed in a later section of the XAS results. The unit cell volume (V) also decreased from 83.272(2) (x = 0) to 81.296 (1) Å^3 (x = 0.20) with increasing x, suggesting the solid solution form. The composition of each compound

Table 1. Refined lattice parameters for P2–$Na_{0.7}[(Fe_{0.5}Mn_{0.5})_{1-x}Co_x]O_2$ powders (x = 0, 0.05, 0.10, and 0.20).

x in P2–$Na_{0.7}[(Fe_{0.5}Mn_{0.5})_{1-x}Co_x]O_2$	a [Å]	c [Å]	V [Å^3]
x = 0.00	2.92225 (2)	11.2598 (2)	83.272 (2)
x = 0.05	2.91552 (2)	11.2504 (1)	82.819 (1)
x = 0.10	2.90852 (2)	11.2409 (1)	82.353 (1)
x = 0.20	2.89233 (2)	11.2213 (2)	81.296 (1)

Table 2. Crystallographic parameters of P2–$Na_{0.7}Fe_{0.4}Mn_{0.4}Co_{0.2}O_2$ refined by the Rietveld method. The refined lattice parameters of the impurity phase are $a = 2.9459$ (2) Å, $c = 16.517$ (6) Å in the *R-3m* space group (No. 166). The refined weight fraction of the P2 and O3 phases are 97.75 (1) and 2.25 (8), respectively. ($R_p = 9.18\%$, $R_{wp} = 11.89\%$, $R_B = 11.90\%$, $\chi^2 = 1.93$).

Atom	Wyckoff	*x*	*y*	*z*	Occupancy	$U_{iso} \times 100$
Na1	2*b*	0	0	1/4	0.23 (1)	2.7 (4)
Na2	2*c*	2/3	1/3	3/4	0.36 (1)	4.9 (4)
Fe1	2*a*	0	0	0	0.4	1.80 (3)
Mn1	2*a*	0	0	0	0.4	1.80 (3)
Co1	2*a*	0	0	0	0.2	1.80 (3)
O1	4*f*	2/3	1/3	0.0861 (2)	0.99 (1)	1.42 (11)

was determined by inductively coupled plasma-atomic emission spectroscopy (ICP-AES), and was close to the expected compositions (Table S1, Supporting Information). The scanning electron microscopy (SEM) images of the powder samples with four compositions ($Na_{0.7}Fe_{0.5}Mn_{0.5}O_2$, $Na_{0.7}Fe_{0.475}Mn_{0.475}Co_{0.05}O_2$, $Na_{0.7}Fe_{0.45}Mn_{0.45}Co_{0.1}O_2$, and $Na_{0.7}Fe_{0.4}Mn_{0.4}Co_{0.2}O_2$) are shown in the inset of Figure S1 (Supporting Information). The particle morphology consisted of hexagonal platelets, and the typical particle size varied from 1 to 2 µm for each compound.

The electrochemical properties of P2–$Na_{0.7}[(Fe_{0.5}Mn_{0.5})_{1-x}Co_x]O_2$ (x = 0, 0.05, 0.10, and 0.20) were tested with electrolytes of 1 M $NaClO_4$ in PC with 2 vol% fluoroethylene carbonate (FEC) at a current rate of 10 mA g^{-1}. All compounds of P2–$Na_{0.7}[(Fe_{0.5}Mn_{0.5})_{1-x}Co_x]O_2$ (x = 0, 0.05, 0.10, and 0.20) exhibited two differential capacity (dQ/dV) peaks over a voltage range of 1.5–4.5 V, as shown in **Figure 2**a. The peaks in the low voltage region (≈2 V) shifted to a lower potential, and the peaks in the high voltage region (>3.5 V) shifted to a higher potential with increasing Co contents. There is a large voltage difference between the positive (oxidation) peak and negative (reduction) peak in the high voltage region, whereas only small differences were observed in the low voltage region. This indicates high polarization in the higher voltage region. This observation will be discussed in more detail in the in situ XRD investigation. Figure 2b shows the initial charge/discharge voltage profiles for four P2 layered materials. All the samples exhibited similar discharge capacities of ≈190 mAh g^{-1}. However, the discharge voltage plateau at ≈3.5 V increased with increasing amounts of

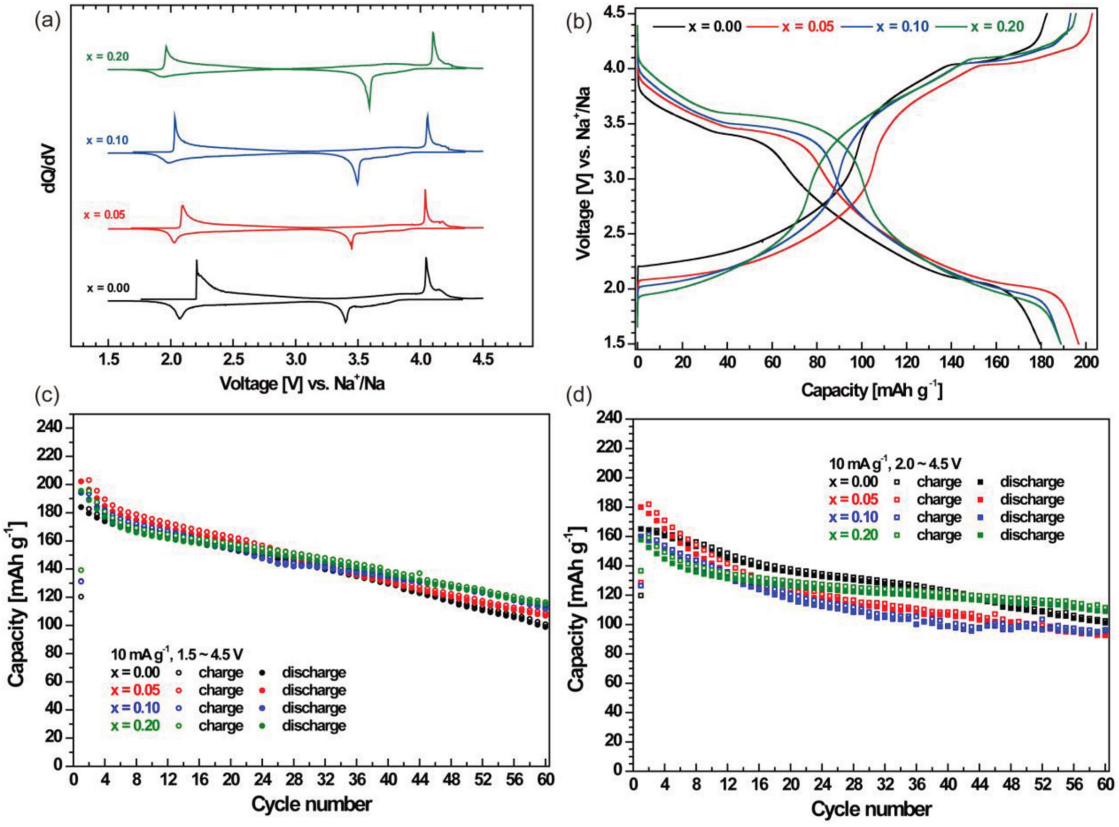

Figure 2. a) The dQ/dV plots, b) capacity versus voltage profiles, and c) capacity retention at 10 mA g^{-1} from 1.5 to 4.5 V and d) from 2.0 to 4.5 V for P2–$Na_{0.7}[(Fe_{0.5}Mn_{0.5})_{1-x}Co_x]O_2$ materials (x = 0, 0.05, 0.10, and 0.20).

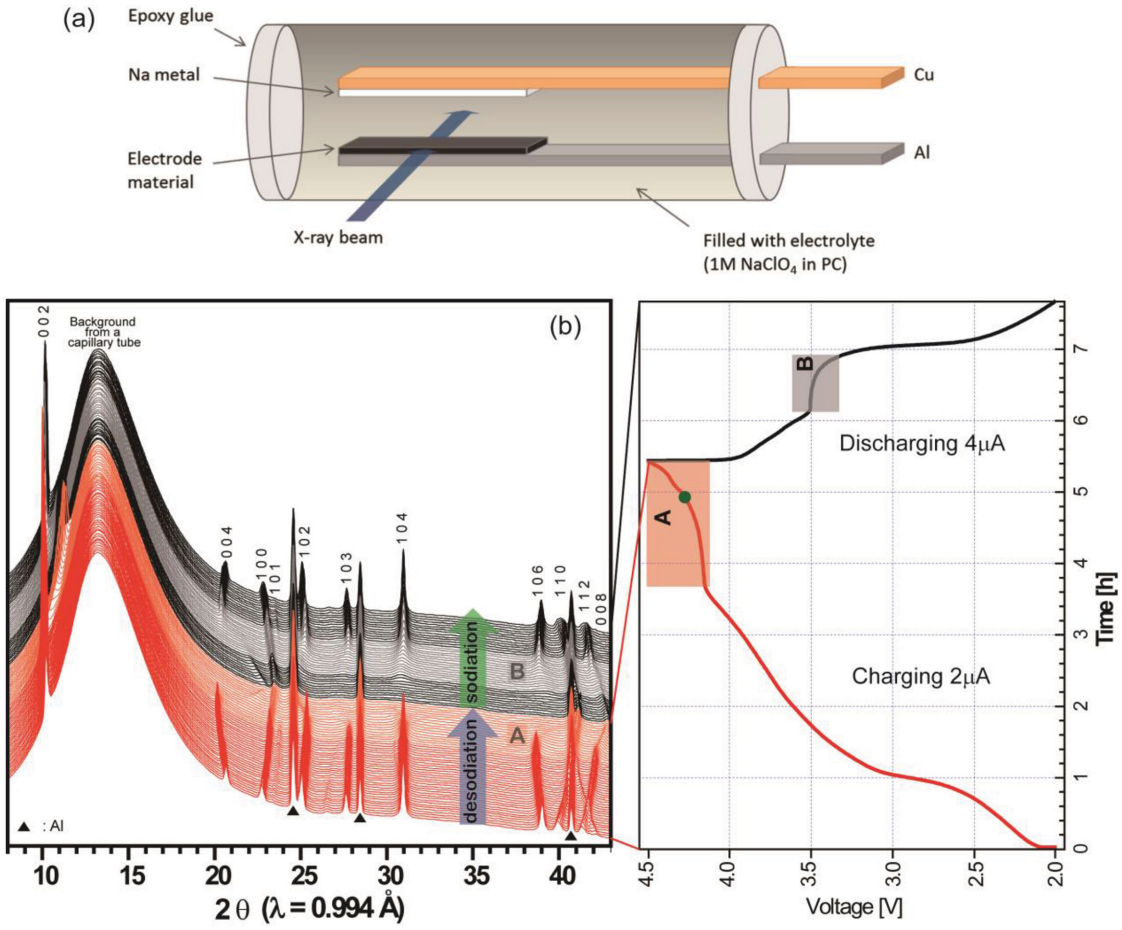

Figure 3. a) Schematic illustration of a capillary-based microbattery cell with a P2–$Na_{0.7}Fe_{0.4}Mn_{0.4}Co_{0.2}O_2$ electrode. b) In situ synchrotron XRD patterns of the P2–$Na_{0.7}Fe_{0.4}Mn_{0.4}Co_{0.2}O_2$ electrode while an Na//$Na_{0.7}Fe_{0.4}Mn_{0.4}Co_{0.2}O_2$ capillary cell was charged at a current of 2 μA to 4.5 V and discharged at a current of 4 μA to 2.0 V.

Co, which is in agreement with the dQ/dV plots. Figure 2c,d shows cycling performances for P2–$Na_{0.7}[(Fe_{0.5}Mn_{0.5})_{1-x}Co_x]O_2$ (x = 0, 0.05, 0.10, and 0.20) in different voltage ranges at a current of 10 mA g^{-1}. The initial Coulombic efficiency at voltages of 1.5–4.5 V was ≈98% but gradually increased and reached 99% by 60 cycles. Cycling tests at a charge of 4.5 V versus Na^+/Na also included electrolyte decomposition. Although the overall cyclability of the four samples was similar, the capacity retention with higher Co contents was more stable. In particular, $Na_{0.7}Fe_{0.4}Mn_{0.4}Co_{0.2}O_2$ delivered a high capacity of ≈115 mAh g^{-1} after 60 cycles. Therefore, $Na_{0.7}Fe_{0.4}Mn_{0.4}Co_{0.2}O_2$ was selected as a model for P2–$Na_{0.7}[(Fe_{0.5}Mn_{0.5})_{1-x}Co_x]O_2$ materials to further investigate the relationship between the crystal structure of the electrode materials and electrochemical properties.

2.2. In Situ Synchrotron X-Ray Diffraction

In situ synchrotron XRD measurements of P2–$Na_{0.7}Fe_{0.4}Mn_{0.4}Co_{0.2}O_2$ were carried out to confirm the exact phase change of the P2–$Na_{0.7}[(Fe_{0.5}Mn_{0.5})_{1-x}Co_x]O_2$ materials during electrochemical desodiation and sodiation. **Figure 3**a shows the schematic design of a capillary-based microbattery cell for in situ investigation during electrochemical cycling. The capillary cell was first charged and discharged at a current of 4 μA in a voltage of 4.5–2.0 V versus Na^+/Na, subsequently charged to 4.5 V at a current of 2 μA, and discharged to 2.0 V at a current of 4 μA in the second cycle. Figure 3b shows a plot of the in situ synchrotron XRD patterns collected during the second cycle of the P2–$Na_{0.7}Fe_{0.4}Mn_{0.4}Co_{0.2}O_2$ material. The XRD patterns obtained during charging (scan No. 1–49, one per 400 s) and discharging (scan No. 50–88, one per 200 s) are presented in red and black, respectively. The (0 0 4) peak at ≈21° shifted continuously to a lower angle during the initial charge from 2.0 to 4.1 V, indicating expansion of the slab thickness on desodiation. In contrast, the (1 0 0) peak moved to a higher angle because of the decrease in the TM–TM distance with the deintercalation of sodium ions. The oxidation of transition metals with smaller ionic radii supposedly leads to the contraction of the *ab* plane, maintaining the P2 structure. This indicates a solid–solution behavior before reaching the voltage plateau at ≈4.1 V. During the discharge process, the opposite tendency occurs after the voltage plateau at ≈3.5 V, and the peaks revert to their original positions.

A significant change in the in situ diffraction data during charging occurred in region A (the plateau above 4.1 V).

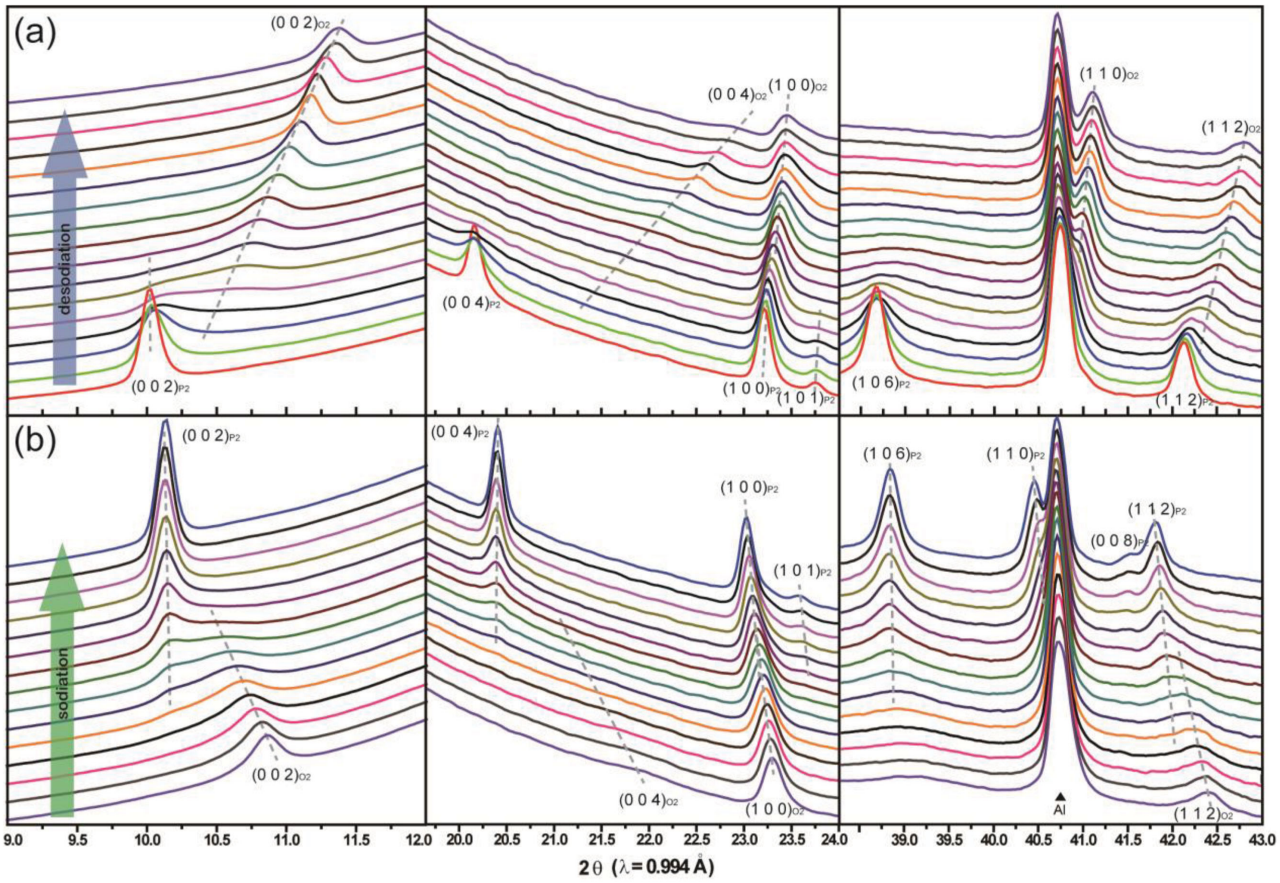

Figure 4. Magnified in situ synchrotron XRD patterns in a) region A (desodiation) and b) region B (sodiation) in Figure 3. The primary peak changes show reversible phase transitions during electrochemical charge and discharge processes.

Figure 4a,b presents magnified regions of A (from scan No. 33 to 49) and B (from scan No. 61 to 75), which were marked in Figure 3b. The (0 0 2) and (0 0 4) peaks of the original phase shifted slightly to higher angles, accompanied by a decrease in the peak intensity and an increase in the peak broadness. During the subsequent charging process, the (0 0 2) and (0 0 4) peaks of the O2 phase arose at a higher 2θ value, which corresponds to a structural transition from P2 to O2 in this region. After the coexisting region of the two phases, only the O2 phase remained at the end of the plateau. The (0 0 2) peak of the O2 phase moved noticeably to higher angles from further desodiation to a fully charged state, while the (1 0 0) and (1 1 0) peaks of the O2 phase shifted slightly to higher angles. The reverse behavior for the O2 phase is also observed in Figure 4b, suggesting a reversible reaction for the structural phase transition.

The cell parameters (*a*, *c*, and *V*) of each scan number that correspond to the voltage profile of P2–$Na_{0.7}Fe_{0.4}Mn_{0.4}Co_{0.2}O_2$ are shown in **Figure 5**. The cell parameters for the P2 phase were refined with the Rietveld method, starting from the $P6_3/mmc$ space group identical to the powder sample. The lattice parameter *a* (corresponding to the TM–TM distance within the TMO_2 slabs) decreased continuously during charging due to the decrease in the average ionic radii of transition metals from their oxidation, whereas the lattice parameter *c* (corresponding to the TMO_2 slab thickness) increased gradually due to electrostatic repulsion between oxygen ions during sodium extraction. The continuous changes in cell parameters are indicative of a single-phase reaction with a solid–solution behavior, and the total lattice volume contraction of the P2 phase was 2.1% before reaching the voltage plateau at 4.1 V. Shaded regions reveal the biphasic domain (e.g., two-phase region) where the P2 structure transforms into another layered structure and vice versa, which matches the layered O2 structure. The initial structural model for the O2 phase was adopted from O2–$LiCoO_2$[35] with space group $P6_3mc$ (No. 186). In the two-phase region, peaks for original P2 showed a gradual decrease in intensity compared to increasing peaks for the O2 phase. The cell parameters for P2 and O2 in the transition regions (marked in yellow in Figure 5) were not very well determined because of the disordered structure resulting in broad reflections. The cell parameters for the O2 phase were determined by Le Bail fitting because noticeable diffraction peaks are limited for conducting a structural refinement in the O2 phase. Figure S2 (Supporting Information) displays the Le Bail fitting result of an XRD pattern for the green dot (scan No. 38) in region A of Figure 3b.

Only the O2 phase remained as the desodiation process continued past the two-phase region, and the lattice parameter *c* in the O2 phase rapidly decreased to that in the P2 phase. Such a sharp change in *c* has also been observed in the O2 structure, which transformed from P2–$Na_{2/3}[Ni_{1/3}Mn_{2/3}]$

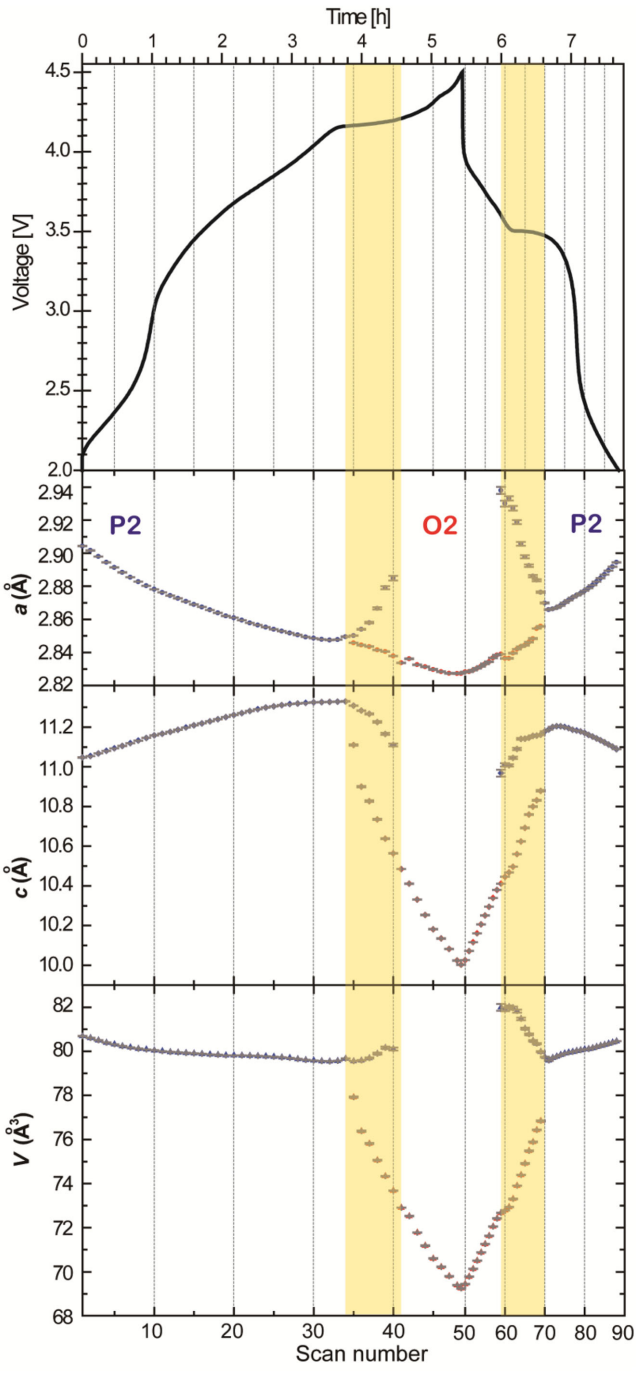

Figure 5. Variations in cell parameters and phase evolution of the P2–$Na_{0.7}Fe_{0.4}Mn_{0.4}Co_{0.2}O_2$ electrode fitted by in situ synchrotron XRD patterns. The corresponding voltage profile of the Na//$Na_{0.7}Fe_{0.4}Mn_{0.4}Co_{0.2}O_2$ capillary cell is shown for comparison.

O_2 after desodiation.[17,21] The lattice parameter c of O2–$Na_{2/3}[Ni_{1/3}Mn_{2/3}]O_2$ at the fully charged state has been reported as ≈9.0 Å, smaller than the value of 10.00 (2) Å in the current work. The overall lattice volumes for both P2 and O2 decreased as Na was extracted, but the variation in the O2 phase was much larger (from 77.92 (3) to 69.25 (2) $Å^3$) than that of the P2 phase (from 81.30 (1) to 79.54 (1) $Å^3$), resulting in severe volume contraction of the lattice toward a fully charged state. Conversely, lattice parameters a and c in the O2 phase continuously increased during discharge until the electrode reached the two-phase region (region B in Figure 3b). The original P2 structure was restored after phase transformation from O2 to P2 during the sodiation process, and the variation in the cell parameters of the P2 phase exhibited the opposite trend to the charging step, indicating a reversible phase transition of the electrode.

The amount of Na ions during the in situ measurement was approximated electrochemically; ≈0.1 Na ions remained in the fully charged state, while ≈0.77 (≈160 mAh g^{-1}) Na ions could be reinserted into P2–$Na_yFe_{0.4}Mn_{0.4}Co_{0.2}O_2$ (Figure S3, Supporting Information). Combining the in situ XRD and galvanostatic cycling results, the O2 phase was formed when the remaining Na ions were ≈1/3 in the initial P2 structure, indicating that the P2–O2 phase transition occurred at the plateau above 4.1 V. This result is in agreement with other P2 layered materials,[17,21] where the O2 structure is formed through the gliding of TMO_2 layers as Na ions are deintercalated from the prismatic sites. The GITT measurement (Figure S3b, Supporting Information) also supports the phase-transition behavior of P2–$Na_{0.7}Fe_{0.4}Mn_{0.4}Co_{0.2}O_2$. The sloping curve up to 4.1 V with low polarization is the signature of solid–solution behavior and exactly matched the continuous peak shifts in the XRD patterns maintaining the original P2 structure. The O2 phase region with a large overpotential implies that layered O2 with small amounts of Na ions is unstable, and $Na_yFe_{0.4}Mn_{0.4}Co_{0.2}O_2$ ($y \approx 0.1$) with an O2 phase at the fully charged state can therefore not be obtained directly.

Crystal structures for P2 and O2 are displayed in **Figure 6**a. Presumably, the gliding of TMO_2 slabs without breaking the TM–O bonding leads to octahedral sites for Na ions. The O2 phase has a hexagonal close-packed (hcp) oxygen array; therefore, it is generally formed as a layered structure with stacking faults along the c-axis after transition from the P2 phase through extraction of Na ions.[21] This phenomenon has also been reported for O2 Li layered structures prepared by ion exchanging P2 structure layered sodium manganese oxides.[36] Le Bail fitting results of the fully charged state (scan No. 49) presented an absence of (1 0 l) diffractions peaks for $Na_yFe_{0.4}Mn_{0.4}Co_{0.2}O_2$ (Figure 6b). A gradual broadening of the (1 0 l) diffraction peaks for the P2 phase was observed, and (1 0 l) peaks for the O2 phase were barely observed because of high stacking faults resulting from the ordering of transition metals.[9,37]

As Na ions are extracted, the gliding of the TMO_2 sheets would induce a structural change from prismatic to octahedral sites and thereby result in a large lattice contraction (Figure 5). Le Bail fitting results exhibited a volumetric contraction from P2 to O2 of 14.8%, whereas the change within the P2 single phase was only 2.1%. This large volume change from P2 to O2 during desodiation can lead to increased stresses and thereby result in gradual capacity fading during cycling. Although the Na-ion mobility in the P2 structure is faster than that in the O3 structure,[17–20] the kinetic limitation from the gliding transitions between the oxygen layers could affect the overall electrochemical performance, as inferred by in situ XRD. In light of this, galvanostatic cycling over limited

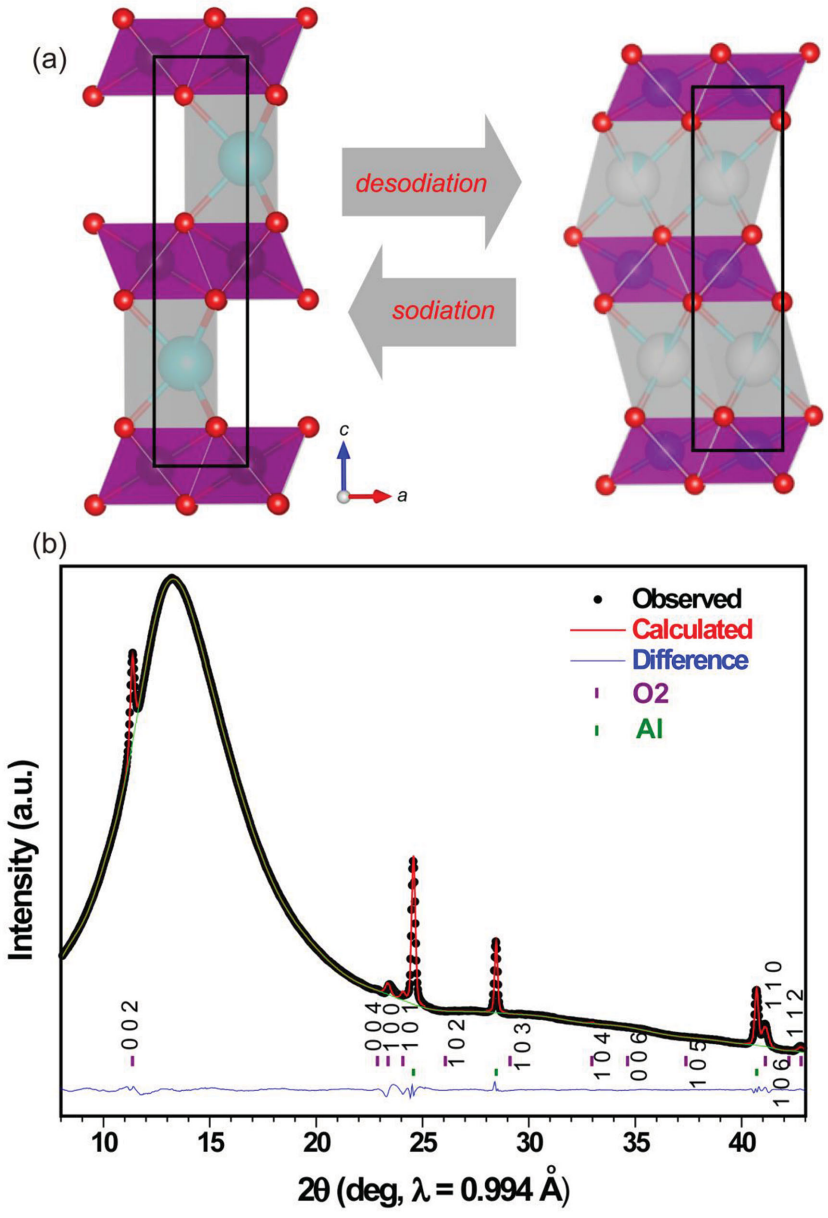

Figure 6. a) Crystal structures of the P2 and O2 phases after sodium extraction. b) The Le Bail fitting result for $Na_yFe_{0.4}Mn_{0.4}Co_{0.2}O_2$ with an O2 structure at the fully charged state (4.5 V).

voltage regions was performed to suppress structural changes (Figure S4, Supporting Information). The cycling performance of P2–$Na_{0.7}Fe_{0.4}Mn_{0.4}Co_{0.2}O_2$ at 10 mA g^{-1} in a voltage range of 2.0–4.0 V demonstrated enhanced cyclability by 140 cycles compared to that in a wide voltage range including phase transformations. Despite the lower value of the initial capacity (≈100 mAh g^{-1}) due to utilization of limited Na ions, high Coulombic efficiencies above 99.5% were achieved. Smooth voltage profiles during cycling within a narrow range also indicate a single-phase reaction without biphasic transitions. Figure S4c,d (Supporting Information) shows the cyclability and voltage curves of P2–$Na_{0.7}[(Fe_{0.5}Mn_{0.5})_{1-x}Co_x]O_2$ (x = 0, 0.1, and 0.2) in a narrow voltage window. The average discharge voltage increased as 2.72, 2.82, and 2.96 V, with x = 0, 0.1, and 0.2, respectively. Additionally, the capacity retention of Co-substituted samples was shown to be stable under no structural transitions. We further tested the rate performance of P2–$Na_{0.7}Fe_{0.4}Mn_{0.4}Co_{0.2}O_2$ between 1.25 and 4.1 V at different current rates (Figure S5, Supporting Information). The discharge capacity of the P2–$Na_{0.7}Fe_{0.4}Mn_{0.4}Co_{0.2}O_2$ decreased to 142, 111, 94, 80, and 57 mAh g^{-1} when the current rate was increased to 20, 50, 100, 200, and 500 mA g^{-1}, respectively. Compared to other P2 layered materials (i.e., $Na_{2/3}Fe_{1/3}Mn_{1/3}Co_{1/3}O_2$[31] and $Na_{0.7}Mn_{0.6}Ni_{0.3}Co_{0.1}O_2$[27], the rate capability of P2–$Na_{0.7}Fe_{0.4}Mn_{0.4}Co_{0.2}O_2$ was comparable, and a higher capacity of 57 mAh g^{-1} was obtained at a high rate of 500 mA g^{-1}.

2.3. Ex Situ X-Ray Absorption Spectroscopy

Ex situ XAS experiments were conducted to investigate the corresponding redox behavior of each transition metal in electrochemical reactions with P2–$Na_{0.7}Fe_{0.4}Mn_{0.4}Co_{0.2}O_2$. **Figure 7** shows the X-ray absorption near-edge structure (XANES) spectra of Fe, Mn, and Co K-edge during charge and discharge processes of P2–$Na_{0.7}Fe_{0.4}Mn_{0.4}Co_{0.2}O_2$. The Mn, Fe, and Co K-edge XANES spectra shift at the edge position toward higher energies with increasing oxidation states of transition metals during the charging states and reverse shift toward a lower energy after the discharging steps. However, major shifts in the XANES spectra for each transition metal were somewhat different, as magnified in the insets of Figure 7a,c,e.

The Fe K-edge (7112 eV) XANES spectrum was clearly moved to a higher energy after oxidation to 3.7 V, and the shape and intensity of spectra at higher energies were slightly different. Fe^{3+} ions are likely partially oxidized, but the degree of oxidation cannot be accurately confirmed because P2–$Na_{0.7}Fe_{0.4}Mn_{0.4}Co_{0.2}O_2$ cannot be maintained in the fully charged state (4.5 V) by ex situ measurements (Figure S6, Supporting Information). Nevertheless, an obvious change was observed in the pre-edge region, where the pre-edge peak gradually became larger by continuous charging to 4.2 V and disappeared under 3.6 V during discharge. This is in agreement with the previous XANES results for the layered compound containing Fe^{3+} and Fe^{4+}.[9] Thorne et al. also reported that oxidation from Fe^{3+} to Fe^{4+} occurs at higher voltages than 4.1 V in $Na_{2/3}Fe_{1/3}Mn_{1/3}Co_{1/3}O_2$, which was confirmed by Mössbauer spectroscopy.[30] Distorted Fe^{4+} octahedra showed a large pre-edge peak, while Fe^{3+} octahedra exhibited a negligible pre-edge peak due to much weaker transitions. The unusual Fe^{4+} ions during desodiation in the upper

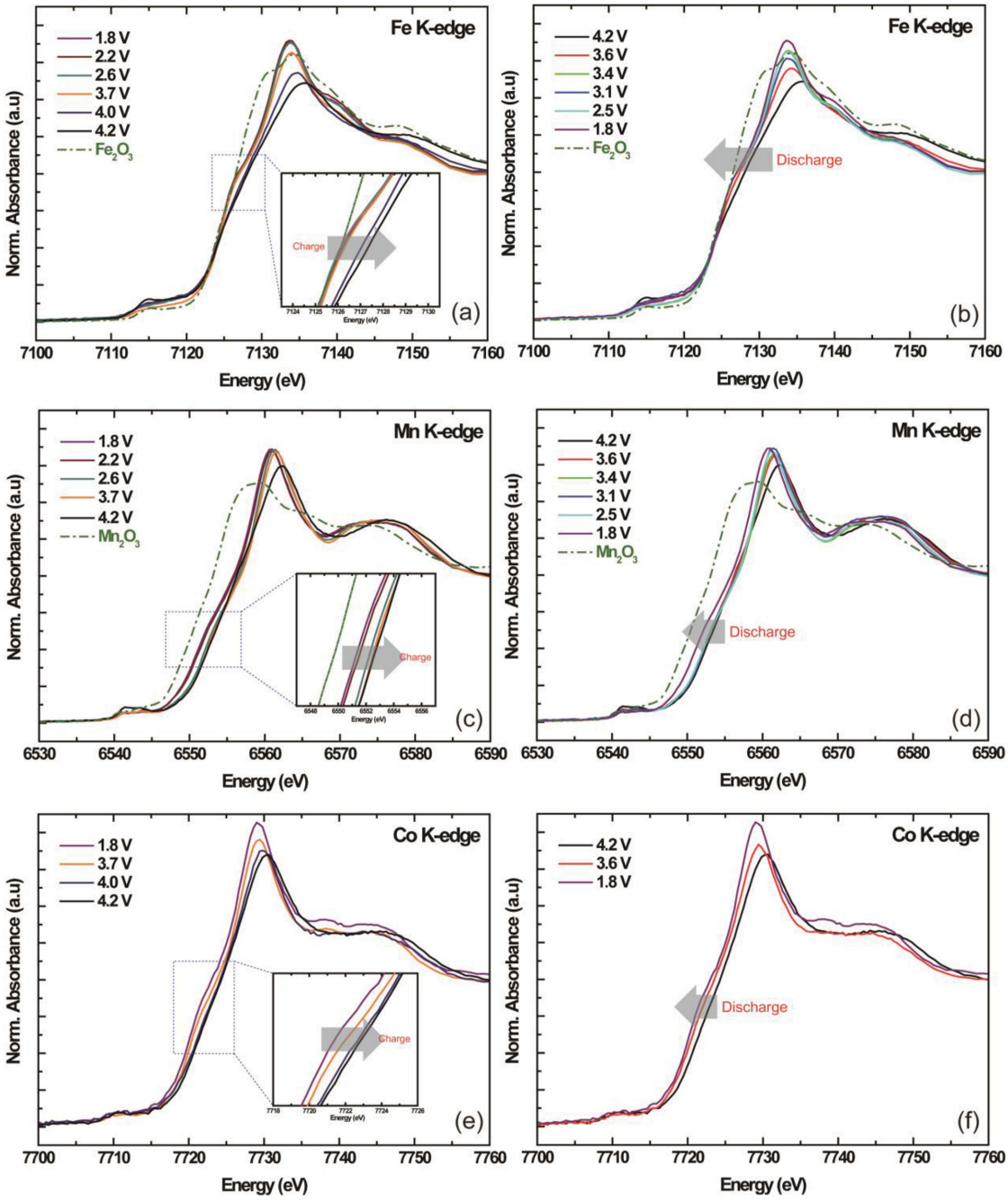

Figure 7. XANES spectra at a,b) the Fe K-edge, c,d) the Mn K-edge, and e,f) the Co K-edge during sodium deintercalation and intercalation process.

voltage region might have affected the voltage hysteresis of the P2–$Na_{0.7}[(Fe_{0.5}Mn_{0.5})_{1-x}Co_x]O_2$ materials.[38,39]

In the Mn K-edge (6539 eV) spectrum, both Mn^{3+} and Mn^{4+} coexisted in P2–$Na_{0.7}Fe_{0.4}Mn_{0.4}Co_{0.2}O_2$, as expected from Na-deficient P2 material. The XANES spectrum was shifted significantly during oxidation to 2.6 V, whereas a slight shift from 2.6 to 4.2 V was found at the Mn K-edge. This is consistent with recent publications on P2–$Na_xFe_yMn_{1-y}O_2$; the main redox couple in the lower voltage region below 4 V was $Mn^{3+/4+}$, while the Fe^{3+} was oxidized to the unstable Fe^{4+} at a higher potential.[40] Figure 7e,f shows the Co K-edge (7709 eV) XANES spectra of P2–$Na_{0.7}Fe_{0.4}Mn_{0.4}Co_{0.2}O_2$ during charging and discharging. The spectrum was shifted over the entire range during the electrochemical reaction, but the variation was narrow after oxidation to 4.0 V. The oxidation state for Co could not be determined because of the absence of reference materials for Co, but it was estimated to be between Co^{3+} and Co^{4+}.

The k^3-weighted Fourier-transform (FT) magnitude of the Fe and Mn K-edges extended X-ray absorption fine structure (EXAFS) spectra for P2–$Na_{0.7}Fe_{0.4}Mn_{0.4}Co_{0.2}O_2$ during cycling is shown in **Figure 8**. Two intense peaks in both the Fe and Mn K-edges appeared in the range of 1–3 Å, which are ascribed

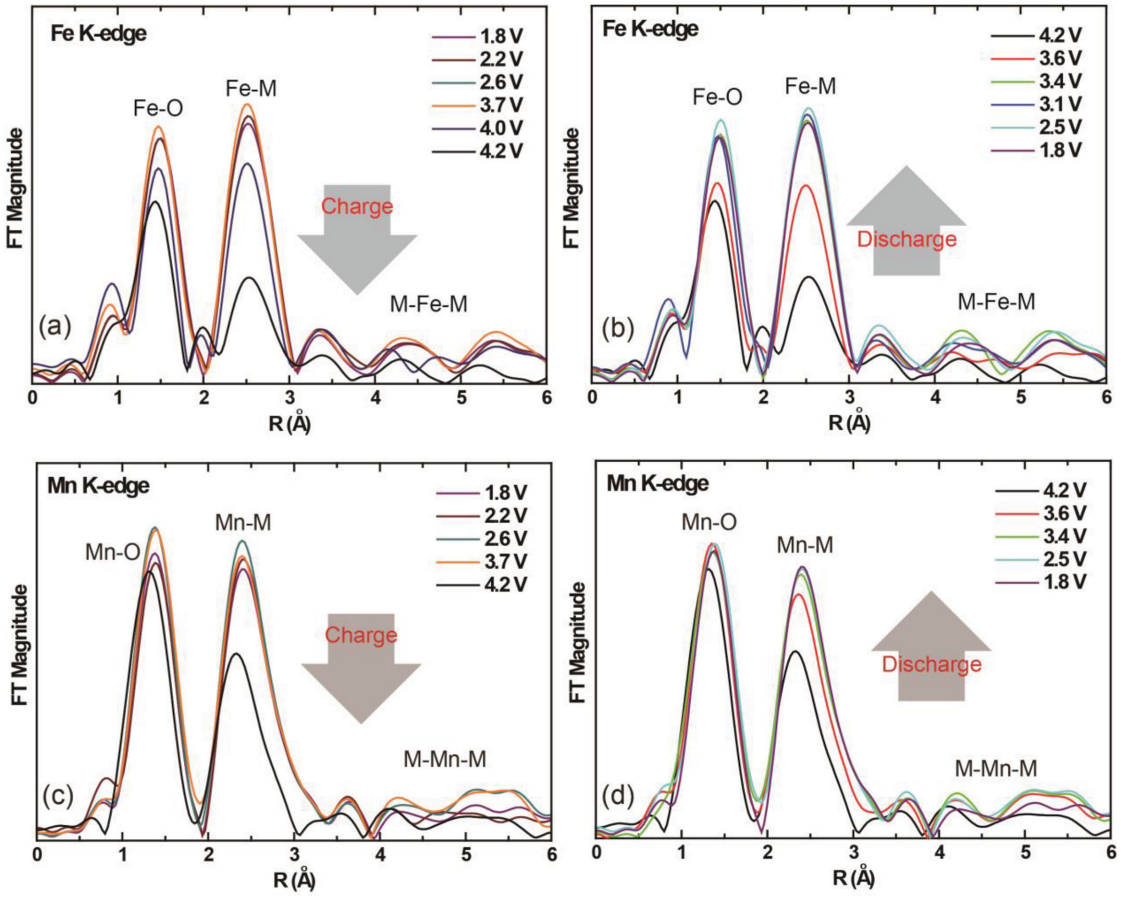

Figure 8. Fourier-transformed EXAFS spectra collected at a,b) the Fe K-edge and c,d) the Mn K-edge.

to TM–O and TM–TM coordination, respectively. In the Fe K-edge EXAFS spectra, both the interatomic distance of Fe–O and the FT magnitude decreased upon charge because of the oxidation of Fe, especially in the high voltage region (>3.7 V). In particular, the complex shape at 4.2 V implies strong local distortion of the adjacent FeO_6 octahedra, suggesting instability of Fe^{4+} charging over 3.7 V.[41] On the contrary, the Mn K-edge EXAFS spectra showed no noticeable change in overall shape except for the spectrum at 4.2 V. The lower FT magnitude of Mn–TM at the Mn K-edge might have been affected by local distortion of adjacent Fe atoms at a higher potential. Consequently, Mn^{3+} was first oxidized in a lower potential region, and Fe^{3+} was oxidized in the higher potential region during charging of P2–$Na_{0.7}Fe_{0.4}Mn_{0.4}Co_{0.2}O_2$. Due to the large size of Fe^{3+} ions, these ions were compressed in their octahedra, and there was a strong tendency to reduce the Fe–O distance upon extraction of Na. Partial oxidation of Fe occurred in a highly charged state. Simultaneously, the Jahn–Teller effect coupled to Na ordering for Fe^{4+} and Mn^{3+} could also influence a gradual degradation of the P2–$Na_{0.7}[(Fe_{0.5}Mn_{0.5})_{1-x}Co_x]O_2$ materials[42] associated with a structural transition. As seen in the previous dQ/dV result, the solid–solution range widened slightly as the Co content increased in P2–$Na_{0.7}[(Fe_{0.5}Mn_{0.5})_{1-x}Co_x]O_2$. Combining the XANES results with electrochemistry, the addition of Co could expand the single-phase region by replacement of Co into Fe (the high voltage region), as well as Mn (the low voltage region), resulting in the extent of the solid solution domain.

3. Conclusions

P2–$Na_{0.7}[(Fe_{0.5}Mn_{0.5})_{1-x}Co_x]O_2$ (x = 0, 0.05, 0.10, and 0.20) was synthesized through solid-state reaction as a positive electrode material for sodium-ion batteries. The synchrotron X-ray diffraction patterns showed that the majority phase of the as-synthesized powders was indexed as a hexagonal P2 layered structure. All dQ/dV plots showed two corresponding redox peaks, but the overall operating voltage was varied slightly through Co substitution. P2–$Na_{0.7}Fe_{0.4}Mn_{0.4}Co_{0.2}O_2$ was selected as a model for P2–Fe–Mn–Co layered materials to investigate the structural change during electrochemical reactions by synchrotron-based in situ XRD and ex situ XAS. In situ synchrotron XRD analysis of an electrochemical Na-ion capillary cell in transmission mode showed a phase transformation from P2 to O2 after a plateau at ≈4.1 V. However, the original P2 structure was completely restored under the following sodiation processes. The structural transition from P2 to O2 occurred by gliding of the TMO_2 sheets, accompanied by a volumetric contraction of ≈15% in the lattice during desodiation. This large change in volume during desodiation/sodiation can lead to increased stress and

thereby result in gradual capacity loss after continuous cycling. The ex situ XAS results for P2–$Na_{0.7}Fe_{0.4}Mn_{0.4}Co_{0.2}O_2$ indicate corresponding redox behaviors of each transition metal. The absorption energy for the Fe K-edge primarily shifted to higher positions after charging above 3.7 V, but the Mn K-edge absorption spectrum exhibited a major shift below 2.6 V. The current study could provide a broader view of the structural behaviors of the P2 layered structure during electrochemical reactions.

4. Experimental Section

Synthesis of the P2 Layered Materials: P2–$Na_{0.7}[(Fe_{0.5}Mn_{0.5})_{1-x}Co_x]O_2$ (x = 0, 0.05, 0.10, and 0.20) was synthesized via a solid-state reaction from a stoichiometric mixture of Na_2CO_3 (Aldrich), Fe_3O_4 (Samchun), Co_3O_4 (Aldrich), and Mn_3O_4 (Aldrich). A 5 wt% excess of Na_2CO_3 was added to compensate for the evaporation of sodium during the synthesis. The reaction mixtures were ground in an agate mortar, pressed into 15 mm diameter pellets, and heated at 900 °C for 15 h in air. The cooling rate was 1 °C min^{-1}, and the pellet was transferred to a glove box at 300 °C.

Characterization: The XRD patterns for as-synthesized powder samples were obtained using synchrotron XRD at the 9B-HRPD beamline (λ = 1.4647 Å) at Pohang Accelerator Laboratory (PAL) in Pohang, Korea. Synchrotron PXRD data were collected at room temperature with a six multidetector system over an angular range of $10° \leq 2\theta \leq 130.5°$ at a 0.01° step width. The crystal structure was refined using the powder profile refinement program GSAS[43] with EXPGUI.[44] A pseudo-Voigt function was used to fit the line shape of the diffraction peaks. The following parameters were refined in the final runs: the unit cell parameter, scale factor, background, displacement shift, pseudo-Voigt function corrected for asymmetry parameters, positional coordinates, isotropic thermal factors, and occupancy of Na. The ratio of transition metals was fixed. The morphology and microstructure were characterized using scanning electron microscopy (FE-SEM, Philips, XL-30). The atomic ratios of Na, Fe, Co, and Mn of the layered materials were determined using ICP-AES (Thermo Scientific, iCAP 6300 Duo).

Electrochemical Testing: The electrodes used for electrochemical testing were prepared by mixing P2 layered materials, carbon black (Super-P, Timcal), and polymer binder (PVdF, Aldrich) in a weight ratio of 80:10:10 on aluminum foils. The electrode was dried at 120 °C under vacuum overnight. The loading of the active material was ≈1–2 mg cm^{-2}. CR2032 coin cells were assembled to characterize the performance of the electrodes using Na metal as the counter and reference electrodes in an Ar-filled glove box ([H_2O] and [O_2] < 1 ppm). The Na metal (Cubes, Aldrich) was initially cleaned with hexane (anhydrous, Aldrich) to remove mineral oil and was then cut, rolled, and punched out. The electrolyte was 1 M $NaClO_4$ in propylene carbonate (PC) with 2 vol% of FEC,[45] and polypropylene (PP) membranes (Celgard 2400) were used as separators. The galvanostatic intermittent titration technique (GITT) was conducted at a current of 10 mA g^{-1} for 0.5 h with a 2 h relaxation time using a VMP3 potentiostat (Bio-Logic), and galvanostatic cycling tests were performed using a WBCS3000 cycler (Wonatech). All measurements were conducted at ambient temperature.

Preparation of a Capillary-Based Cell for In Situ Experiments: A capillary-based microbattery[46] was prepared for in situ experiments. The slurry of $Na_{0.7}Fe_{0.4}Mn_{0.4}Co_{0.2}O_2$ was prepared by the same method as mentioned above and was deposited on the tip of a thin flat Al stick. The electrodes were transferred to a glove box and dried under vacuum overnight at 120 °C to remove all residual water. A small piece of Na metal was cut and placed on a Cu stick as an anode. The sticks were placed in a glass capillary with a width of 1 mm and a height of 4 mm, fixed by epoxy adhesive and dried overnight in an Ar-filled glove box. The capillary cell was then filled with liquid electrolyte (1 M $NaClO_4$ in PC) and finally sealed by epoxy adhesive.

In Situ Synchrotron X-Ray Powder Diffraction: In situ synchrotron XRD patterns were obtained to investigate structural changes in $Na_{0.7}Fe_{0.4}Mn_{0.4}Co_{0.2}O_2$ during desodiation and sodiation. The experiments were performed on the MAX-lab I711 beamline in Lund, Sweden. The capillary cell was fixed on a goniometer head using an insulating sample holder frame, and the electrode position was adjusted to be penetrated by X-rays directly. Due to a beam size above 100 μm, diffractions from both the active material and the Al current collector were obtained. The charge/discharge current for the first cycle was 4 μA, and the cell was charged at 2 μA to 4.5 V and discharged at 4 μA to 2.0 V in the second cycle by a potentiostat (VSP-200, Bio-Logic). The time resolution was 25.7 s $scan^{-1}$ in the in situ experiments, and we selected 88 scans in the second cycle for structural analysis among the measured 1768 patterns. We estimated that 1 μA corresponded to ≈20 mA g^{-1} (active material loading of ≈0.05 mg in a capillary cell) in this experiment. Powder diffraction data in transmission mode were collected during charging and discharging using a Titan CCD detector, and a sample-to-detector distance of 70 mm, a wavelength of 0.994 Å, a slit size of 0.2 × 0.2 mm, and an exposure time of 20 s were used. The raw data obtained from a CCD detector were transformed to 2D powder diffraction patterns. The in situ data for the P2 phase in the single-phase region were analyzed using the Rietveld method; the refined parameters were lattice parameters, positional coordinates for the oxygen atom, isotropic thermal factors, and occupancy of Na. The lattice parameters for the O2 phase were determined by Le Bail fitting.

Ex Situ Synchrotron X-Ray Absorption Spectroscopy Measurement: Ex situ XAS for the P2–$Na_{0.7}Fe_{0.4}Mn_{0.4}Co_{0.2}O_2$ electrode was conducted in the transmission and fluorescence modes at the 7D XAFS beamline at PAL. All electrodes charged or discharged to a certain potential as coin cells were disassembled in an Ar-filled glove box for XAS measurements. Fe, Mn, and Co K-edge energy calibrations were performed using Fe, Mn, and Co metal foils as references, respectively. A reference spectrum was simultaneously recorded for the in situ spectrum using reference metal foil. The measurement of the Mn K-edge region was carried out in a He-filled chamber to prevent noise from air. Pre-edge background and post-edge normalization of the Fe, Mn, and Co K-edge spectra were performed using the ATHENA software.[47]

Supporting Information

Supporting Information is available from the Wiley Online Library or from the author.

Acknowledgements

This work was supported by the Program to Solve Climate Changes (NRF-2010-C1AAA001-2010-0029031) through the National Research Foundation of Korea (NRF) funded by the Ministry of Science, ICT & Future Planning. It was also supported by the Climate Change Research Hub of KAIST (Grant No. N01150034). The authors acknowledge technical support from staffs of the I711 beamline at MAX-lab, the 9B-HRPD beamline and the 7D-XAFS at PAL in the experiments.

Received: February 4, 2015
Revised: March 17, 2015
Published online: April 15, 2015

[1] V. Palomares, M. Casas-Cabanas, E. Castillo-Martinez, M. H. Han, T. Rojo, *Energy Environ. Sci.* **2013**, *6*, 2312.
[2] M. D. Slater, D. Kim, E. Lee, C. S. Johnson, *Adv. Funct. Mater.* **2013**, *23*, 947.
[3] S. Y. Hong, Y. Kim, Y. Park, A. Choi, N. S. Choi, K. T. Lee, *Energy Environ. Sci.* **2013**, *6*, 2067.
[4] H. L. Pan, Y. S. Hu, L. Q. Chen, *Energy Environ. Sci.* **2013**, *6*, 2338.

[5] N. Yabuuchi, K. Kubota, M. Dahbi, S. Komaba, *Chem. Rev.* **2014**, *114*, 11636.
[6] D. Larcher, J. M. Tarascon, *Nat. Chem.* **2015**, *7*, 19.
[7] K. Kubota, N. Yabuuchi, H. Yoshida, M. Dahbi, S. Komaba, *MRS Bull.* **2014**, *39*, 416.
[8] M. H. Han, E. Gonzalo, G. Singh, T. Rojo, *Energy Environ. Sci.* **2015**, *8*, 81.
[9] N. Yabuuchi, M. Kajiyama, J. Iwatate, H. Nishikawa, S. Hitomi, R. Okuyama, R. Usui, Y. Yamada, S. Komaba, *Nat. Mater.* **2012**, *11*, 512.
[10] M. Sathiya, K. Hemalatha, K. Ramesha, J.-M. Tarascon, A. S. Prakash, *Chem. Mater.* **2012**, *24*, 1846.
[11] P. Vassilaras, A. J. Toumar, G. Ceder, *Electrochem. Commun.* **2014**, *38*, 79.
[12] S. M. Oh, S. T. Myung, J. Y. Hwang, B. Scrosati, K. Amine, Y. K. Sun, *Chem. Mater.* **2014**, *26*, 6165.
[13] J. H. Cheng, C. J. Pan, J. F. Lee, J. M. Chen, M. Guignard, C. Delmas, D. Carlier, B. J. Hwang, *Chem. Mater.* **2014**, *26*, 1219.
[14] J. Xu, D. H. Lee, Y. S. Meng, *Funct. Mater. Lett.* **2013**, *6*, 1330001.
[15] C. Delmas, C. Fouassier, P. Hagenmuller, *Phys. B* **1980**, *99*, 81.
[16] C. Delmas, J. J. Braconnier, C. Fouassier, P. Hagenmuller, *Solid State Ionics* **1981**, *3*, 165.
[17] D. H. Lee, J. Xu, Y. S. Meng, *Phys. Chem. Chem. Phys.* **2013**, *15*, 3304.
[18] Y. S. Wang, X. Q. Yu, S. Y. Xu, J. M. Bai, R. J. Xiao, Y. S. Hu, H. Li, X. Q. Yang, L. Q. Chen, X. J. Huang, *Nat. Commun.* **2013**, *4*, 2365.
[19] S. Kim, X. H. Ma, S. P. Ong, G. Ceder, *Phys. Chem. Chem. Phys.* **2012**, *14*, 15571.
[20] Y. F. Mo, S. P. Ong, G. Ceder, *Chem. Mater.* **2014**, *26*, 5208.
[21] Z. H. Lu, J. R. Dahn, *J. Electrochem. Soc.* **2001**, *148*, A1225.
[22] D. Carlier, J. H. Cheng, R. Berthelot, M. Guignard, M. Yoncheva, R. Stoyanova, B. J. Hwang, C. Delmas, *Dalton Trans.* **2011**, *40*, 9306.
[23] X. F. Wang, M. Tamaru, M. Okubo, A. Yamada, *J. Phys. Chem. C* **2013**, *117*, 15545.
[24] J. Xu, D. H. Lee, R. J. Clement, X. Q. Yu, M. Leskes, A. J. Pell, G. Pintacuda, X. Q. Yang, C. P. Grey, Y. S. Meng, *Chem. Mater.* **2014**, *26*, 1260.
[25] J. Billaud, G. Singh, A. R. Armstrong, E. Gonzalo, V. Roddatis, M. Armand, T. Rojo, P. G. Bruce, *Energy Environ. Sci.* **2014**, *7*, 1387.
[26] D. Buchholz, A. Moretti, R. Kloepsch, S. Nowak, V. Siozios, M. Winter, S. Passerini, *Chem. Mater.* **2013**, *25*, 142.
[27] J. Yoshida, E. Guerin, M. Aranault, C. Constantin, B. M. Boisse, D. Carlier, M. Guignard, C. Delmas, *J. Electrochem. Soc.* **2014**, *161*, A1987.
[28] D. D. Yuan, W. He, F. Pei, F. Y. Wu, Y. Wu, J. F. Qian, Y. L. Cao, X. P. Ai, H. X. Yang, *J. Mater. Chem. A* **2013**, *1*, 3895.
[29] S. Doubaji, M. Valvo, I. Saadoune, M. Dahbi, K. Edstrom, *J. Power Sources* **2014**, *266*, 275.
[30] D. D. Yuan, X. H. Hu, J. F. Qian, F. Pei, F. Y. Wu, R. J. Mao, X. P. Ai, H. X. Yang, Y. L. Cao, *Electrochim. Acta* **2014**, *116*, 300.
[31] J. S. Thorne, R. A. Dunlap, M. N. Obrovac, *J. Electrochem. Soc.* **2014**, *161*, A2232.
[32] N. Yabuuchi, S. Komaba, *Sci. Technol. Adv. Mater.* **2014**, *15*, 043501.
[33] G. Prado, L. Fournes, C. Delmas, *J. Solid State Chem.* **2001**, *159*, 103.
[34] P. Suresh, A. K. Shukla, N. Munichandraiah, *J. Power Sources* **2006**, *159*, 1395.
[35] J. M. Paulsen, J. R. Mueller-Neuhaus, J. R. Dahn, *J. Electrochem. Soc.* **2000**, *147*, 508.
[36] J. M. Paulsen, C. L. Thomas, J. R. Dahn, *J. Electrochem. Soc.* **1999**, *146*, 3560.
[37] J. Breger, M. Jiang, N. Dupre, Y. S. Meng, Y. Shao-Horn, G. Ceder, C. P. Grey, *J. Solid State Chem.* **2005**, *178*, 2575.
[38] Y. Takeda, K. Nakahara, M. Nishijima, N. Imanishi, O. Yamamoto, M. Takano, R. Kanno, *Mater. Res. Bull.* **1994**, *29*, 659.
[39] N. Yabuuchi, H. Yoshida, S. Komaba, *Electrochemistry* **2012**, *80*, 716.
[40] J. Zhao, J. Xu, D. H. Lee, N. Dimov, Y. S. Meng, S. Okada, *J. Power Sources* **2014**, *264*, 235.
[41] N. Yabuuchi, M. Yano, H. Yoshida, S. Kuze, S. Komaba, *J. Electrochem. Soc.* **2013**, *160*, A3131.
[42] X. Li, X. H. Ma, D. Su, L. Liu, R. Chisnell, S. P. Ong, H. L. Chen, A. Toumar, J. C. Idrobo, Y. C. Lei, J. M. Bai, F. Wang, J. W. Lynn, Y. S. Lee, G. Ceder, *Nat. Mater.* **2014**, *13*, 586.
[43] A. C. Larson, R. B. Von Dreele, *Los Alamos National Laboratory Report LAUR*, **2004**, p. 86.
[44] B. H. Toby, *J. Appl. Crystallogr.* **2001**, *34*, 210.
[45] S. Komaba, T. Ishikawa, N. Yabuuchi, W. Murata, A. Ito, Y. Ohsawa, *ACS Appl. Mater. Interfaces* **2011**, *3*, 4165.
[46] A. S. Christiansen, R. E. Johnsen, P. Norby, C. Frandsen, S. Mørup, S. H. Jensen, K. K. Hansen, P. Holtappels, *J. Electrochem. Soc.* **2015**, *162*, A531.
[47] B. Ravel, M. Newville, *J. Synchrotron Radiat.* **2005**, *12*, 537.